

Precise and Robust Domain Engineering Based on Faraday Cage Effect for Thin-film Lithium Niobate Photonics

YANQUN WANG,¹ FURONG ZHONG,¹ LIN LIU,¹ YUNTAO ZHU,¹ JINYI WANG,¹ ZHONGJIN LIN,^{1,3} AND XINLUN CAI^{1,2,4}

¹State Key Laboratory of Optoelectronic Materials and Technologies, School of Electronics and Information Technology, Sun Yat-sen University, Guangzhou 510275, China

²Hefei National Laboratory, Hefei 230088, China

³linzhj56@mail.sysu.edu.cn

⁴caixlun5@mail.sysu.edu.cn

Abstract: Thin-film lithium niobate (TFLN) waveguides are promising for efficient second-harmonic generation (SHG) owing to their strong optical confinement and large second-order nonlinearity. However, robust fabrication of high-efficiency devices remains challenging, as existing domain engineering methods lack precise and robust controls of polarity distributions. Here, we propose and demonstrate a domain engineering technique that utilizes nanoscale Faraday cages to shape the electric-field distributions during poling, physically defining polarity distribution by the geometry of the Faraday cages without real-time monitoring. As a proof of concept, the method is used to fabricate a spatially selectively poled TFLN waveguide, where all regions are poled except for a 400-nm-wide central. This waveguide achieves a normalized SHG efficiency of 6242 %W⁻¹cm⁻². Systematic investigation of the inverted domain growth dynamics confirms the enhanced precision and robustness of this approach over conventional time-controlled methods, paving the way for scalable nonlinear photonic circuits.

1. Introduction

Efficient second-harmonic generation (SHG) is essential for advancing classical and quantum photonic technologies [1-9]. Various integrated photonic material platforms have been explored to achieve a high SHG efficiency[10-15]. In particular, the thin-film lithium niobate (TFLN) integrated photonic platform stands out due to its large $\chi^{(2)}$ nonlinearity, flexible domain engineering, and strong optical confinement[13, 14, 16-28]. Despite significant progress has been achieved through advanced domain engineering techniques[5, 13, 29-34], achieving consistently high SHG efficiency with robust fabrication remains difficult due to stringent requirements for phase-matching conditions.

Electric-field poling—the dominant method for domain inversion—relies on applying a strong electric field to reorient ferroelectric domains[29, 35-37]. However, the evolution of domain inversion under electric fields involves complex dynamics[36, 37]. Once an electric field stronger than the coercive field is applied to a TFLN waveguide, inverted domains rapidly expand between the electrodes within tens of milliseconds[29]. This high-speed process makes precise control of the final polarity distribution particularly challenging, as even slight variations in the inverted-domain growth rate can lead to substantial deviations from the target pattern. The inverted-domain growth rate is highly sensitive to material properties and poling conditions, including LN conductivity, electrode–LN contact resistance, temperature, and humidity[37]. Although in-situ monitoring is commonly employed to guide the poling process[29, 35], it cannot compensate for stochastic effects, such as surface defects, adsorbed charges, or electrode imperfections[35, 37-39]. These stochastic effects can randomly create domain nucleation, resulting in nonuniform expansion of the inverted domains. To the best of our knowledge, no electric-field poling method has been able to effectively address this challenge[37], highlighting the need for further efforts toward the robust fabrication of high-efficiency devices.

Here, we propose and demonstrate a domain engineering technique based on the Faraday cage effect. Nanoscale metal structures are used to locally shape the electric field during poling, physically defining unpoled regions by geometry rather than by critical timing. As a proof of concept, we fabricate a spatially selectively poled TFLN (SSP-TFLN) waveguide, enabling modal phase matching (MPM) between the TE_{00} fundamental mode and the TE_{20} second-harmonic mode, with a normalized SHG conversion efficiency of $6242\%W^{-1}cm^{-2}$. We further investigate the spatial and temporal dynamics of inverted-domain growth, and confirm that the proposed approach enables robust fabrication of TFLN waveguides with high SHG conversion efficiency. The proposed method can also be used to fabricate other types of SHG TFLN waveguides, such as double-layer TFLN waveguides or other ferroelectric material waveguides. This work opens a new avenue for highly efficient and scalable nonlinear photonics.

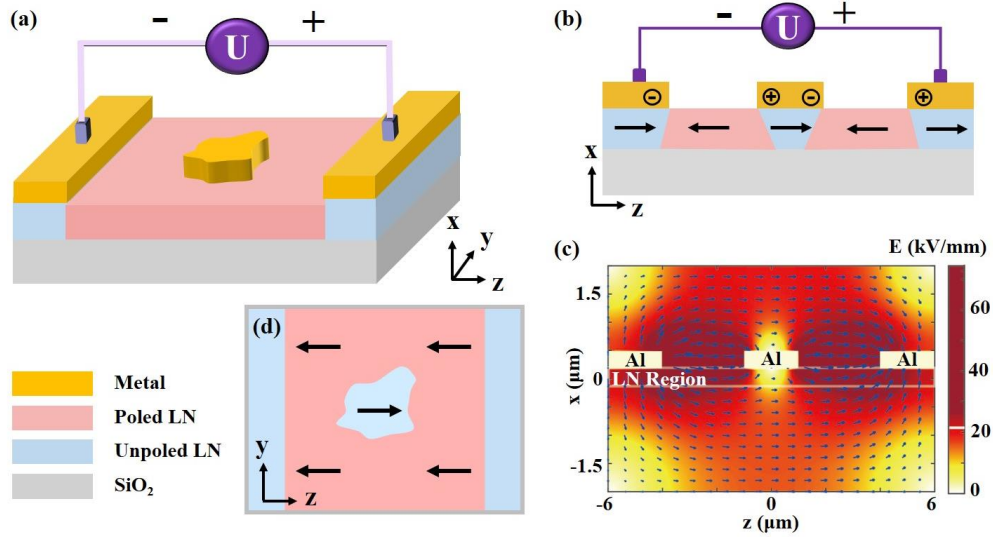


Fig. 1. (a) Schematic of electric-field poling principle (b) Cross-section of electric-field poling principle on $x-z$ plane. (c) E-field distribution on the $x-z$ plane. (d) The polarity distribution on the surface of lithium niobate (LN) film after removal of the metal electrode.

2. Concept and Principle

The fundamental principle of the Faraday-cage-based poling method is presented in Figs. 1(a) and 1(b). A voltage applied across electrodes generates an external electric field along the negative direction of z -axis. A nano-metal structure with any patterns between the electrodes acts as a Faraday cage: free charges redistribute under the external electric field, screening the interior and reshaping the surrounding field, as illustrated by the cross-sectional electric-field distribution in Fig. 1(c). The redistributed free charges locally suppress the field beneath the nano-metal structure, preventing domain inversion there while allowing poling elsewhere. The unpoled and poled regions (*i.e.*, polarity distributions) are thus precisely defined by the nano-metal patterns (see Fig. 1(d)).

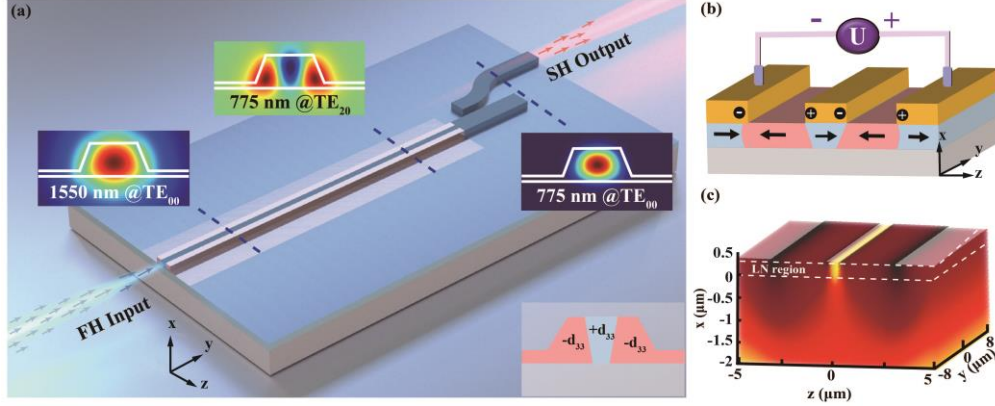


Fig. 2. (a) Schematic of the spatially selectively poled-thin film lithium niobate (SSP-TFLN) waveguide structure for efficient SHG via precise domain control technology. Three insets display the simulated cross-sectional electric field profiles at three representative positions: the input TE_{00} mode at 1550 nm, the generated TE_{20} mode at 775 nm within the poled region, the output TE_{00} mode at 775 nm. Right bottom inset shows the domain engineered waveguide cross-section. (b) Schematic of electric-field poling principle for second-harmonic generation (SHG). (c) Three-dimensional E-field distribution for SHG.

To demonstrate the capability of the proposed poling method, an SSP-TFLN waveguide is selected as a representative structure and fabricated on a 360-nm-thick x-cut LN film. Notably, the proposed method is applicable to LN films with other thicknesses as well. The choice of the 360-nm-thick x-cut LN film is primarily dictated by our process design kit (PDK), which enables monolithic integration of the nonlinear components with other photonic elements, facilitating the realization of more complex and powerful systems in the future. As shown in Fig. 2(a), all domains in the SSP-TFLN waveguide are poled except for a nano-wide strip at the center. This configuration requires extremely precise control of the polarity distribution and cannot be achieved using conventional electric-field poling methods. The SSP-TFLN waveguide creates the nonlinear polarity profile required for MPM between the TE_{00} FH light and the TE_{20} SH light, maximizing the nonlinear mode overlap integral, thereby significantly enhancing the conversion efficiency. A mode converter at the output side extracts the SH light from the bus waveguide and converts it to the TE_{00} mode. To fabricate the SSP-TFLN waveguide, a nano-metal strip is introduced between the electrodes, as shown in Fig. 2(b). Simulated electric-field distributions confirm that the electric field beneath the nano-metal strip is effectively suppressed (see Fig. 2(c)), enabling realization of the SSP-TFLN structure.

3. Device design

According to the MPM theoretical model, the normalized SHG conversion efficiency of the proposed SSP-TFLN waveguide at a FH wavelength, λ_{SH} , can be given by,

$$\eta = \frac{8\pi^2 d_{eff}^2}{\epsilon_0 c n_{FH}^2 n_{SH} \lambda_{FH}^2 A_{eff}} \zeta^2 \text{sinc}^2 \left(\frac{2\pi(n_{FH} - n_{SH})L}{\lambda_{FH}} \right) \quad (1)$$

where n_{FH} and n_{SH} are the effective refractive indices of the FH and SH light, respectively. ϵ_0 and c are the vacuum permittivity and speed of light in vacuum, respectively. A_{eff} , L , and d_{eff} represent effective nonlinear interaction areas, waveguide length, and effective nonlinear coefficient, respectively. ζ is the mode overlap factor between the TE_{00} FH mode and TE_{20} SH mode, given by

$$\zeta = \frac{\left| \int_{\chi(z)} d(x,z) (E_{z,FH})^* E_{z,SH} dx dz \right|}{\left[\int_{\chi(z)} d(x,z) |E_{z,FH}|^2 E_{z,FH} dx dz \right]^{2/3} \left[\int_{\chi(z)} d(x,z) |E_{z,SH}|^2 E_{z,SH} dx dz \right]^{1/3}} \quad (2)$$

where $d(x, z)$ represents the $\chi^{(2)}$ polarity distribution of waveguide cross-section, and takes values of -1 and 1 in the poled and unpoled regions of the waveguide, respectively. E_{FH} and E_{SH} denote the electric field of the FH and SH optical modes, respectively. Equations (1)- (2) indicate that the normalized SHG conversion efficiency can be significantly improved by decreasing $|n_{FH} - n_{SH}|$ and increasing ζ^2 .

$|n_{FH} - n_{SH}|$ can be optimized by the width of waveguide (see Fig. 3(a)). Here, we set the thicknesses of the total and slab layers at 360 nm and 50 nm, respectively. Figure 3a shows that $|n_{FH} - n_{SH}|$ achieves a minimum value (*i.e.*, zero) when the width of waveguide, W_{LN} , equals to 0.68 μm . When the waveguide geometry is fixed, the polarity distribution $d(x, z)$ becomes the primary factor governing the ζ , and consequently the efficiency η . The polarity distribution can be optimized by adjusting the size of the nano-metal structure. Here, the $d(x, z)$ is derived from the electric-field distribution. When the local electric field exceeds the coercive field, the ferroelectric domain orientation is inverted, resulting in a sign reversal of $d(x, z)$. Accordingly, the sign of $d(x, z)$ is determined by whether the local electric field is above or below the coercive field.

Figure 3(b) presents the mode overlap factor ζ and normalized SHG conversion efficiency as a function of the nano-metal width, W_{Al} . The simulations reveal that the efficiency peaks at a width of 400 nm, where optimal mode overlap is achieved. Figure 3(c) compares the simulated efficiencies of the poled and unpoled waveguides, showing that the proposed SSP-TFLN achieves a normalized SHG conversion efficiency of 9510 $\%W^{-1}\text{cm}^{-2}$, which is 21.4 dB higher than that of the unpoled waveguide. Here, the mode overlap factors for the unpoled and SSP-TFLN waveguides are 0.077 and 0.78, respectively.

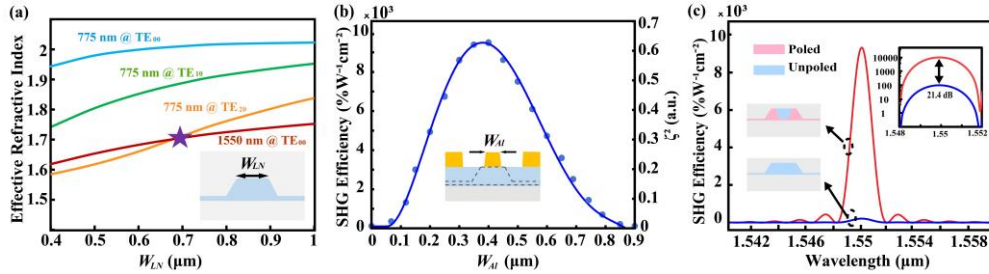


Fig. 3. (a) Dispersion curves for the TE_{00} to TE_{20} modal phase-matching scheme in a thin-film lithium niobate (TFLN) waveguide with a thickness of 360 nm. The insets show the waveguide profiles. (b) Calculated the nonlinear interaction area A_{eff} and Normalized conversion efficiency as functions of the width of the nano-metal (W_{Al}). (c) Theoretical SHG spectral response for the spatially selectively poled-TFLN (SSP-TFLN) and unpoled TFLN waveguides. The left inset shows the corresponding simulated electric field distributions, where blue and red regions denote field strengths below and above the coercive field of TFLN, respectively. The right inset replots the data with a logarithmic scale to highlight the enhanced contrast.

4. Inverted Domain growth

To validate that the nano-metal structure geometrically defines the unpoled region, we studied the inverted domain growth dynamics of the poling process using piezoelectric force microscopy (PFM), as shown in Fig. 4(a). A 150-V, 50Hz rectangular voltage wave are applied to the metal electrodes for poling. The poled domain continues to expand from the positive electrode to the negative electrode except for the regions beneath the nano-metal structure, confirming that the size of the unpoled domain region is determined by the geometry of the nano-metal structure. Although the domain growth is initially nonuniform, the poled domains eventually become uniform and fully occupy the space between the electrodes and the nano-metal strip when a sufficiently large number of voltage pulses is applied. Therefore, the proposed method enables precise control of both poled and unpoled domain sizes without the

need for any in-situ monitoring. Figure 4(b) presents the unpoled width versus poling pulse count, further demonstrating the robustness of the proposed domain engineering method. The cross-sectional PFM image shown in the inset of Fig. 4(b) confirms the presence of a 400 nm unpoled region beneath the metal, which agrees well with the simulated polarity distribution presented in Fig. 3(c).

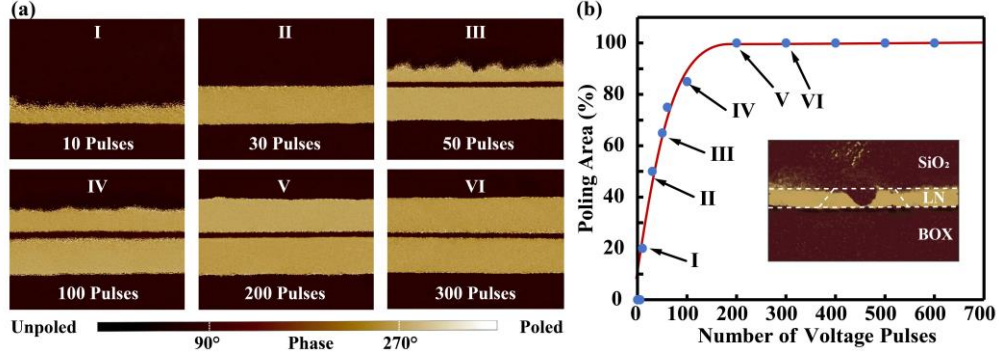


Fig. 4. (a) The horizontal Piezoresponse force microscopy (PFM) phase images at a fixed voltage of 150 V and a frequency of 50 Hz for different number of poling cycles. (b) Poled region width as a function of the number of cycles (poling time). The right insert reveals the cross-sectional PFM of the selective poling through the film. LN, lithium niobate; BOX, buried oxide layer.

5. SHG characterization

The fabrication of the proposed SSP-TFLN waveguide includes three processes: 1) Patterning the metallic structures on the top of lithium niobate (LN) films; 2) Poling the domain orientations of LN with high voltage; 3) Removing the metallic structure and patterning the waveguide structures. To clarify whether the metal deposition and subsequent removal process introduces additional propagation loss, we compared the propagation losses of waveguides fabricated with and without the metal deposition and removal procedures. No noticeable difference in propagation loss was observed between the two types of waveguides.

Figure 5(a) shows a schematic of the experimental setup used to characterize the second-harmonic-generation (SHG) performance of our fabricated device. A tunable continuous-wave laser serves as the FH light source, and is coupled into SSP-TFLN waveguide by a lensed fiber with a mode field diameter (MFD) of 9.5 μm , a numerical aperture of 1.4, and a working distance of 5-10 μm . The generated SH light at the output is coupled off-chip using another lensed fiber and is measured by an optical power meter equipped with a near-infrared blocking filter to ensure that only visible wavelengths are detected.

Figure 5(b) presents the performance of the fabricated TE_{20} to TE_{00} mode converter, which features an insertion loss of -0.85 dB. Figure 5(c) indicates that the five fabricated 2.5-mm-long SSP-TFLN waveguide achieves a normalized peak conversion efficiency of $6224 \pm 400 \text{ \%W}^{-1}\text{cm}^{-2}$, which is approximately 21.1 dB higher than that of the unpoled waveguide ($48 \text{ \%W}^{-1}\text{cm}^{-2}$). The variation of the measured normalized SHG conversion efficiency with the FH wavelength closely follows a sinc^2 function, which agrees well with the MPM theoretical model shown in Eq.(1). The measured normalized peak SHG conversion efficiency reaches approximately 65% of the theoretical value, which may be attributed to deviations between the actual and simulated $d(x,z)$ profiles, film thickness nonuniformity, and fabrication imperfections.

To further demonstrate the robustness of the proposed Faraday-cage-based domain engineering method, Fig. 5(d) shows the normalized SHG conversion efficiencies of SSP-TFLN waveguides poled with 100, 200, and 300 pulses, respectively (i.e., with different poling durations). All their peak efficiencies are close to $6200 \text{ \%W}^{-1}\text{cm}^{-2}$, indicating that our method

reliably produces high-efficiency SSP-TFLN waveguides without requiring precise control over the withdrawal of the external field, as the unpoled regions are inherently defined by the Faraday-cage patterns. Consequently, the proposed approach can repeatedly and robustly fabricate high-efficiency nonlinear waveguides without the in-situ monitoring required in conventional methods, which significantly limits large-scale fabrication. Moreover, Figs. 4(a) and 5(d) show that the proposed method is immune to nonuniform expansions of inverted domain caused by surface defects, adsorbed charges, and electrode fabrication imperfections, which pose major challenges for conventional methods.

Figure 6 presents the absolute SHG conversion efficiency of the fabricated device. An absolute conversion efficiency of 30% is achieved at a pump power of 190 mW. This efficiency can be further improved by increasing the waveguide length and optimizing the thickness uniformity of the LN film. To minimize the influence of thermal effects and photorefractive limitations, the pump power was swept at a high rate. When the pump power was increased slowly, thermal effects on the SHG output became clearly observable. These effects could be further mitigated in future work through active temperature control.

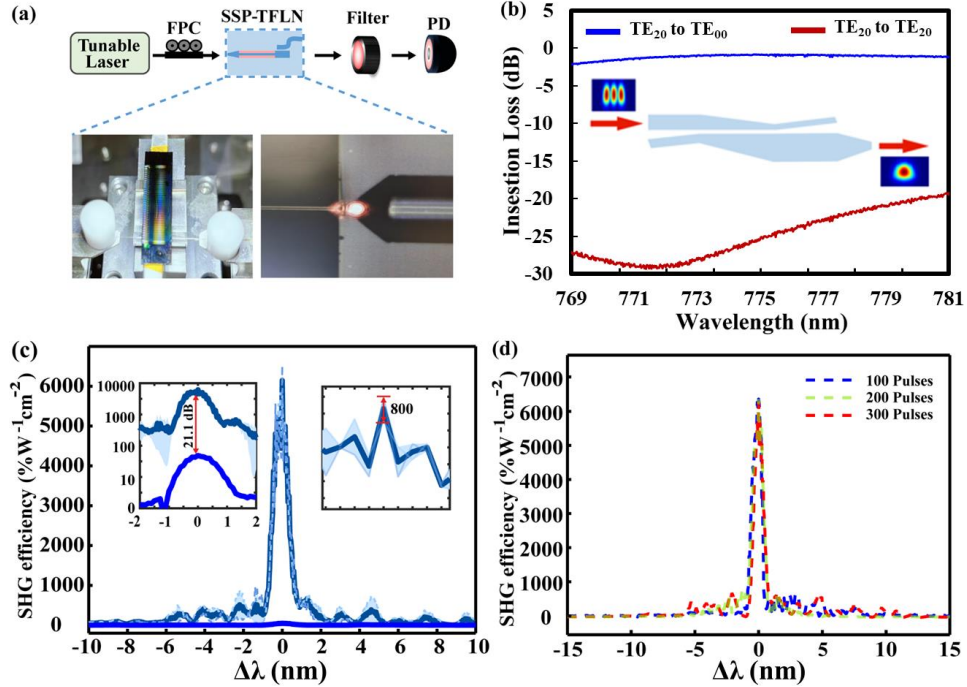


Fig. 5. (a) Schematic of the optical characterization setup. The bottom left inset shows a photograph of the spatially selectively poled-thin film lithium niobate (SSP-TFLN) device under test. The bottom right inset displays the micrograph of the SHG output from the facets of a uniform LN waveguide. (b) Measured transmission performance of the TE_{20} to TE_{00} mode converter. (c) Measured SHG conversion efficiency for the SSP-TFLN and unpoled (conventional) waveguides as a function of pump wavelength. (d) Measured SHG conversion efficiency for the SSP-TFLN with different number of poling cycles.

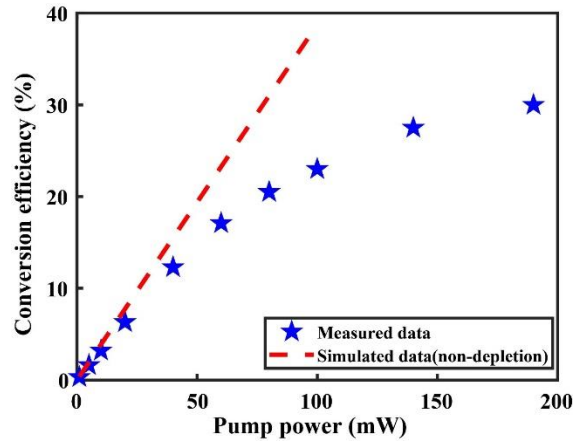


Figure 6 The measured absolute SHG conversion efficiency of the fabricated device varied with pump power.

6. Discussions

The core concept of this work is to physically define the ferroelectric domain distribution through the geometry of the Faraday cages (see Fig. 1). We selected the SSP-TFLN waveguide as a proof-of-concept demonstration because this configuration requires extremely precise control of the polarity distribution, which is highly challenging to achieve using conventional electric-field poling techniques. Although the fabrication of the SSP-TFLN waveguides demonstrates domain control primarily perpendicular to the electrodes, the proposed method enables domain engineering both parallel and perpendicular to the electrodes. Due to space limitations, the application of this method to other waveguide geometries—such as double-layer and periodically poled structures for efficient SHG—will be explored in future work.

7. Conclusions

In summary, we have introduced and experimentally demonstrated, for the first time, a domain engineering method which uses nanoscale Faraday cages to shape the electric field. This approach enables the fabrication of SSP-TFLN waveguides with all regions poled except for a 400-nm-wide central strip. The resulting waveguides demonstrate a normalized SHG conversion efficiency of $6242 \text{ \%W}^{-1}\text{cm}^{-2}$ under continuous-wave fundamental excitation. Strong robustness of the method is confirmed through the studies of spatial and temporal dynamics of the inverted domain growth. While demonstrated here for SSP-TFLN waveguides, the method is broadly applicable to other waveguide geometries, including double-layer and periodically poled structures, for efficient SHG. Overall, this work establishes a new pathway for high-efficiency nonlinear photonics based on precise and robust domain engineering.

Funding. Natural Science Foundation of China (62293523, 62405382); Natural Science Foundation of Guangdong Province, China (2025A1515011473); Quantum Science and Technology-National Science and Technology Major Project(2021ZD0301500); Quantum Science and Technology-National Science and Technology Major Project (2021ZD0300700).

Acknowledgment. This work was supported by the Natural Science Foundation of China (Grants No. 62293523 and 62405382), the Natural Science Foundation of Guangdong Province, China (Grant No. 2025A1515011473), and the Quantum Science and Technology-National Science and Technology Major Project (Grant Nos. 2021ZD0301500 and 2021ZD0300700).

We thank Xiaoyue Liu for support with experimental testing schemes, and Pucheng Huang for the design of the TE₂₀ to TE₀₀ mode converter operating at 775 nm.

Disclosures. The authors declare no conflicts of interest.

Data availability. Data underlying the results presented in this paper may be obtained from the authors upon reasonable request.

References:

1. C. Nabors, et al., *Efficient Second Harmonic Generation Of A Diode-Pumped Cw Nd:YAG Laser Using An Externally Resonant Cavity*, 1988 Los Angeles Symposium: O-E/LASE '88 (SPIE, 1988), Vol. 0898.
2. D. T. Spencer, et al., "An optical-frequency synthesizer using integrated photonics," *Nature* **557**, 81-85 (2018).
3. A. Vaziri, et al., "Experimental two-photon, three-dimensional entanglement for quantum communication," *Physical review letters* **89**, 240401 (2002).
4. J. Zhao, et al., "High quality entangled photon pair generation in periodically poled thin-film lithium niobate waveguides," *Physical review letters* **124**, 163603 (2020).
5. X. Shi, et al., "Efficient photon-pair generation in layer-poled lithium niobate nanophotonic waveguides," *Light: Science Applications* **13**, 282 (2024).
6. J. Lu, et al., "Toward 1% single-photon anharmonicity with periodically poled lithium niobate microring resonators," *Optica* **7**, 1654-1659 (2020).
7. J. Cheng, et al., "Efficient second harmonic generation in a high-Q Fabry-Perot microresonator on x-cut thin film lithium niobate," *Opt. Express* **32**, 12118-12126 (2024).
8. H. Cao, et al., "Photonic source of heralded Greenberger-Horne-Zeilinger states," *Physical Review Letters* **132**, 130604 (2024).
9. L. Deng, et al., "Asymmetrically-Fluorinated Electrolyte Molecule Design for Simultaneous Achieving Good Solvation and High Inertness to Enable Stable Lithium Metal Batteries," *Advanced Energy Materials* **14**, 2303652 (2024).
10. C. Chen, et al., "Design and synthesis of an ultraviolet-transparent nonlinear optical crystal Sr₂Be₂B₂O₇," *Nature* **373**, 322-324 (1995).
11. G. Boyd, et al., "LiNbO₃: an efficient phase matchable nonlinear optical material," *Appl. Phys. Lett.* **5**, 234-236 (1964).
12. D. Cyranoski, "China's crystal cache: a Chinese laboratory is the only source of a valuable crystal. David Cyranoski investigates why it won't share its supplies," *Nature* **457**, 953-956 (2009).
13. C. Wang, et al., "Ultrahigh-efficiency wavelength conversion in nanophotonic periodically poled lithium niobate waveguides," *Optica* **5**, 1438-1441 (2018).
14. R. Luo, et al., "Highly tunable efficient second-harmonic generation in a lithium niobate nanophotonic waveguide," *Optica* **5**, 1006-1011 (2018).
15. L. Gao, et al., "Structure-property survey and computer-assisted screening of mid-infrared nonlinear optical chalcogenides," *Coordination Chemistry Reviews* **421**, 213379 (2020).
16. F. Génèreux, et al., "Deep periodic domain inversions in x-cut LiNbO₃ and its use for second harmonic generation near 1.5 μm," *Appl. Phys. Lett.* **91**(2007).
17. L. Gui, et al., "Local periodic poling of ridges and ridge waveguides on X-and Y-Cut LiNbO₃ and its application for second harmonic generation," *Opt. Express* **17**, 3923-3928 (2009).
18. K. Ravi, et al., "Pulse sequences for efficient multi-cycle terahertz generation in periodically poled lithium niobate," *Opt. Express* **24**, 25582-25607 (2016).
19. J. T. Nagy and R. M. Reano, "Fabricating periodically poled lithium niobate thin films with sub-micrometer fundamental period," in *Laser Science*, (Optica Publishing Group, 2019), JTU3A. 10.
20. A. Rao, et al., "Actively-monitored periodic-poling in thin-film lithium niobate photonic waveguides with ultrahigh nonlinear conversion efficiency of 4600% W⁻¹cm⁻²," *Opt. Express* **27**, 25920-25930 (2019).
21. B. Zhang, et al., "Recent advances in femtosecond laser processing of LiNbO₃ crystals for photonic applications," *Laser Photonics Reviews* **14**, 1900407 (2020).
22. Y. Li, et al., "Recent progress of second harmonic generation based on thin film lithium niobate," *Chinese Optics Letters* **19**, 060012 (2021).
23. M. Younesi, et al., "Periodic poling with a micrometer-range period in thin-film lithium niobate on insulator," *Journal of the Optical Society of America B* **38**, 685-691 (2021).
24. J. He, et al., "Approaching Ideal Second-Harmonic Generation in Polymer Etchless Periodically Poled Thin-Film Lithium Niobate Waveguides with Efficient Domain Characterization," *ACS Photonics* (2025).
25. X. Zhang, et al., "Nonlinear Transverse Mode Conversion Based on Ferroelectric Domain Engineering in Thin Film Lithium Niobate," *Laser Photonics Reviews*, 2500385 (2025).
26. L. Peng, et al., "High-harmonic generation in submicron-thick chirped periodically poled thin-film lithium niobate," *Photonics Res.* **13**, 1917-1924 (2025).
27. Z. Lin, et al., "High-performance polarization management devices based on thin-film lithium niobate," *Light: Science Applications* **11**, 93 (2022).

28. Z. Lin, et al., "120 GOPS Photonic tensor core in thin-film lithium niobate for inference and in situ training," *Nat. Commun.* **15**, 9081 (2024).
29. Y. Niu, et al., "Optimizing the efficiency of a periodically poled LNOI waveguide using in situ monitoring of the ferroelectric domains," *Appl. Phys. Lett.* **116**(2020).
30. X. Liu, et al., "Ultra-broadband and low-loss edge coupler for highly efficient second harmonic generation in thin-film lithium niobate," *Advanced Photonics Nexus* **1**, 016001-016001 (2022).
31. P.-K. Chen, et al., "Adapted poling to break the nonlinear efficiency limit in nanophotonic lithium niobate waveguides," *Nat. nanotechnology* **19**, 44-50 (2024).
32. F. Yang, et al., "Symmetric second-harmonic generation in sub-wavelength periodically poled thin film lithium niobate," *Optica* **11**, 1050-1055 (2024).
33. H. Li, et al., "Nonlinearity Manipulation for Highly Efficient Modal Phase-matched Second Harmonic Generation on Thin-Film Lithium Niobate," *Laser Photonics Reviews* **19**, 2401858 (2025).
34. X. Gu, et al., "Backward second-harmonic generation in periodically poled lithium niobate," *Journal of the Optical Society of America B* **15**, 1561-1566 (1998).
35. Q. Liu, et al., "Ferroelectric Domain Reversal Dynamics in LiNbO₃ Optical Superlattice Investigated with a Real-Time Monitoring System," *Small* **18**, 2202761 (2022).
36. Y. Ishibashi and Y. Takagi, "Note on ferroelectric domain switching," *Journal of the Physical Society of Japan* **31**, 506-510 (1971).
37. V. Y. Shur, "Kinetics of ferroelectric domains: Application of general approach to LiNbO₃ and LiTaO₃," *Journal of Materials Science* **41**, 199-210 (2006).
38. R. G. Batchko, et al., "Backswitch poling in lithium niobate for high-fidelity domain patterning and efficient blue light generation," *Appl. Phys. Lett.* **75**, 1673-1675 (1999).
39. M. J. Missey, et al., "Real-time visualization of domain formation in periodically poled lithium niobate," *Opt. Express* **6**, 186-195 (2000).